

# Cluster Formation of Clay-like Colloids in Shear Flow

Martin Hecht<sup>1</sup>, Jens Harting<sup>1</sup>, and Hans J. Herrmann<sup>2,3</sup>

<sup>1</sup> Institute for Computational Physics, Pfaffenwaldring 27, 70569 Stuttgart, Germany

<sup>2</sup> Institut für Baustoffe, Schafmattstr. 6, ETH Zürich, CH-8093 Zürich, Switzerland

<sup>3</sup> Departamento de Física, Universidade Federal do Ceará Campus do Pici, 60451-970 Fortaleza CE, Brazil

8th February 2020

**Abstract** In  $\text{Al}_2\text{O}_3$  suspensions, depending on the experimental conditions very different microstructures can be found, comprising fluid like suspensions, a repulsive structure, and a clustered microstructure. For technical processing in ceramics, the knowledge of the microstructure is of big importance, since it essentially determines the stability of a workpiece to be produced. To enlighten this topic, we investigate these suspensions by means of a coupled Stochastic Rotation Dynamics (SRD) and Molecular Dynamics (MD) simulation. In the present paper we utilize the structure factor and the pair correlation function as analysis tools to observe cluster formation. The first one observes on the length scale of the system size, whereas the latter focuses on short distances to the nearest neighbours. Both observation tools show good agreement among each other. The repulsive microstructure can be identified by means of the mean squared displacement of the particles. The results from different evaluation tools are summarized in a stability diagram.

**PACS.** 82.70.-y Disperse systems; complex fluids – 47.11.+j Computational methods in fluid dynamics – 02.70.Ns Molecular Dynamics and particle methods

## 1 Introduction

Colloidal suspensions are present everywhere in our daily life. Paintings, cosmetic products, and different kinds of food are some examples. According to their importance a considerable amount of research has been done to describe colloidal suspensions from a theoretical point of view and by simulations [1,2,3,4,5] and to understand the particle-particle interactions [6,7,8,9,10,11], the phase behavior [12,13,14,15], the relevant processes on the microscale and their influence on macroscopic parameters [16,17,18]. Many interesting questions raise and colloid science is a large field of research, with various books reviewing the topic [19,20,21,22]. Colloidal suspensions are in fact complicated systems, since different time and length scales are involved. The particle sizes are on a mesoscopic length scale, i.e. in the range of nanometers up to micrometers. On this length scale observations are easier than on the atomistic length scale. Some effects can already be treated by mean field theories. Brownian motion, often cannot be neglected. Depending on the particle sizes, materials, and concentrations different interactions are of relevance and often several of them are in a subtle in-

terplay: electrostatic repulsion, depletion forces, van der Waals attraction, hydrodynamic interaction, Brownian motion, and gravity are the most important influences. The properties of the suspension are strongly depending on the balance of the microscopic forces between the particles. Especially for industrial processes a detailed understanding of the relevant influences is needed, when one needs to optimize certain material properties. The stability of different microstructures and especially the clustering process are key properties which are of interest.

In our work we investigate these properties, focusing on  $\text{Al}_2\text{O}_3$  particles of diameter  $0.37 \mu\text{m}$  suspended in water. This is a widely used material in ceramics [23,24]. We have developed a simulation code for a Brownian suspension [25]. We have adjusted the simulation parameters so that the simulation corresponds quantitatively to a real suspension and experimental data can be compared directly. The diffusion coefficient, sedimentation velocity [25], and the viscosity of the suspension can be reproduced [26]. For  $\text{Al}_2\text{O}_3$  suspensions attractive van der Waals forces are important for the behavior of this material. Electrostatic repulsion of the charged par-

ticles counteracts the attraction and can prevent clustering depending on the particle surface charge. In Ref. [26] we have presented how one can relate parameters of DLVO potentials [6,7] with experimental conditions. In the experiment one can control the  $pH$ -value and the salt concentration. The latter can be expressed by the ionic strength  $I$ , which is an effective concentration of all ions present in the solution. Both, the  $pH$ -value and the ionic strength, influence the charge of the colloidal particles. We have shown that for not too strongly attractive forces one can obtain reasonable quantitative agreement with experimental results [26].

On these grounds we have explored the stability diagram of  $Al_2O_3$  suspensions. The particles are uncharged close to the so called “isoelectric point” at  $pH = 8.7$ . There, for all ionic strengths the particles form clusters. For lower  $pH$ -values particles can be stabilized in solution, because they are charged. For low  $pH$ -values, low salt concentrations, and high volume fractions a repulsive structure can be found.

The particle size is on a mesoscopic length scale, where Brownian motion is relevant for a correct description. Long range hydrodynamic interactions are important, at least if dynamic effects like shear flow or sedimentation are of interest. A newly developed simulation method, called “Stochastic Rotation Dynamics” (SRD), which includes both, hydrodynamics and Brownian motion, was proposed by Malevanets and Kapral [27,28]. In Ref. [25] we have shown how one can adjust the simulation parameters in a way that quantitative equivalence to a real fluid (like water in our case) can be obtained.

In this paper we extend our investigations to different  $pH$ -values, deeper in the clustered regime, and to the repulsive structure. We know that our model works well, even quantitatively, in the suspended regime of the stability diagram and close to the borders between the different microstructures[26]. Apart from that we expect to gain insight to the microscopic structure on a qualitative level.

In the following section we shortly describe our simulation method. After that we discuss the pair correlation function and the structure factor. The pair correlation function is not directly accessible in experiments, whereas the structure factor can in principle be extracted from scattering data. However, for our suspension scattering experiments are difficult: due to the high volume fraction the beam is multiply scattered. The intensity in light scattering experiments becomes low since the particles are not transparent. For X-ray scattering the particles are large, so that a very small scattering angle has to be chosen. In contrast to that in our simulation, evalua-

tion of the structure factor can easily be done to quantify information about the internal structure, which then can be compared to other works on different materials, where similar effects can be observed more easily. Additionally, we evaluate the so-called demixing parameter  $\Psi$  [29]. To characterize the repulsive region we evaluate the mean squared displacement (MSD), which shows a plateau, if the particle motion consists of different processes acting on well separated time scales. Finally, the results are summarized in a stability diagram for our  $Al_2O_3$ -suspension. It shows the behavior of the suspension in an intuitive way and helps to design industrial processes using this material.

## 2 Simulation method

Our simulation method consists of two parts: a Molecular Dynamics (MD) code, which treats the colloidal particles, and a Stochastic Rotation Dynamics (SRD) simulation for the fluid solvent.

In the MD part of our simulation we include effective electrostatic interactions and van der Waals attraction, known as DLVO potentials [6,7], a lubrication force and Hertzian contact forces. DLVO potentials are composed of two terms, the first one being an exponentially screened Coulomb potential due to the surface charge of the suspended particles

$$V_{\text{Coul}} = \pi \varepsilon_r \varepsilon_0 \left[ \frac{2+\kappa d}{1+\kappa d} \cdot \frac{4k_B T}{ze} \tanh\left(\frac{ze\zeta}{4k_B T}\right) \right]^2 \times \frac{d^2}{r} \exp(-\kappa[r-d]), \quad (1)$$

where  $d$  denotes the particle diameter and  $r$  is the distance between the particle centers.  $e$  is the elementary charge,  $T$  the temperature,  $k_B$  the Boltzmann constant, and  $z$  is the valency of the ions of added salt.  $\varepsilon_0$  is the permittivity of the vacuum,  $\varepsilon_r = 81$  the relative dielectric constant of the solvent.  $\kappa$  is the inverse Debye length defined by  $\kappa^2 = 8\pi\ell_B I$ , with the ionic strength  $I$  and the Bjerrum length  $\ell_B = 7 \text{ \AA}$ . The effective surface potential  $\zeta$  is the electrostatic potential at the border between the diffuse layer and the compact layer. Smoluchowski related it to the electrokinetic mobility of the particle as  $\mu = \zeta\varepsilon_0\varepsilon_r/\eta$  [30]. The  $\zeta$  potential can be related to the  $pH$ -value of the solvent [26].

The Coulomb term competes with the second part of the DLVO potential which is given by the attractive van der Waals interaction

$$V_{\text{vdW}} = -\frac{A_H}{12} \left[ \frac{d^2}{r^2-d^2} + \frac{d^2}{r^2} + 2 \ln\left(\frac{r^2-d^2}{r^2}\right) \right]. \quad (2)$$

$A_H = 4.76 \cdot 10^{-20}$  J is the Hamaker constant [31]. The DLVO potentials exhibit two minima, one primary minimum, where the particles touch each other. Eq. (2) does not describe this minimum, therefore we model the primary minimum by a parabola. The primary minimum is separated by a potential barrier from the secondary minimum, which occurs at larger particle distances and which is less deep. For low salt concentrations, i.e., large Debye screening lengths, the electrostatic repulsion overcompensates the van der Waals attraction and the secondary minimum disappears.

Long range hydrodynamic interactions are taken into account in the simulation for the fluid as described below. This can only reproduce interactions correctly down to a certain length scale. On shorter distances, a lubrication force has to be introduced explicitly in the Molecular Dynamics simulation:

$$\mathbf{F}_{\text{lub}} = -\mathbf{v}_{\text{rel},\perp} \frac{6\pi\eta}{r-d} \left(\frac{d}{4}\right)^2, \quad (3)$$

with the relative velocity  $\mathbf{v}_{\text{rel},\perp}$  projected on the connecting line of the particle centers.  $\eta$  is the dynamic viscosity of the fluid.

To avoid that the particles penetrate each other, we are using a Hertz force described by the potential

$$V_{\text{Hertz}} = K(d-r)^{5/2} \quad \text{if } r < d, \quad (4)$$

where  $K$  is an interaction constant and additionally a damping term

$$\mathbf{F}_{\text{Damp}} = -\mathbf{v}_{\text{rel},\perp} \beta \sqrt{d-r}, \quad (5)$$

with a damping constant  $\beta$ . For the integration of the translational motion we utilize a velocity Verlet algorithm [32].

For the simulation of a fluid solvent, many different simulation methods have been proposed: Stokesian Dynamics (SD) [33,34,3], Accelerated Stokesian Dynamics (ASD) [35,36], pair drag simulations [4], Brownian Dynamics (BD) [31,37], Lattice Boltzmann (LB) [1,2,38,39], and Stochastic Rotation Dynamics (SRD) [40,41,25]. These mesoscopic fluid simulation methods have in common that they make certain approximations to reduce the computational effort. Some of them include thermal noise intrinsically, or it can be included consistently. They scale differently with the number of embedded particles and the complexity of the algorithm differs largely.

We apply the Stochastic Rotation Dynamics method (SRD) introduced by Malevanets and Kapral [27,28]. It intrinsically contains fluctuations, is easy to implement, and has been shown to be well suitable for simulations of colloidal and polymer suspensions [40,41,42,43,44,25,26]

and very recently for star-polymers in shear flow [45]. The method is also known as “Real-coded Lattice Gas” [40] or as “multi-particle-collision dynamics” (MPCD) [46]. It is based on so-called fluid particles with continuous positions and velocities. A streaming step and an interaction step are performed alternately. In the streaming step, each particle  $i$  is moved according to

$$\mathbf{r}_i(t + \tau) = \mathbf{r}_i(t) + \tau \mathbf{v}_i(t), \quad (6)$$

where  $\mathbf{r}_i(t)$  denotes the position of the particle  $i$  at time  $t$  and  $\tau$  is the time step. In the interaction step the fluid particles are sorted into cubic cells of a regular lattice and only the particles within the same cell interact among each other. Interaction means, momentum is exchanged among the particles, but total energy and momentum have to be conserved. The artificial interaction is designed to obey these constraints and to be very simple, i.e., computationally cheap: each cell  $j$  is treated independently. First, the mean velocity  $\mathbf{u}_j(t') = \frac{1}{N_j(t')} \sum_{i=1}^{N_j(t')} \mathbf{v}_i(t)$  is calculated.  $N_j(t')$  is the number of fluid particles contained in cell  $j$  at time  $t' = t + \tau$ . Then, the velocities of each fluid particle in cell  $j$  are rotated according to

$$\mathbf{v}_i(t + \tau) = \mathbf{u}_j(t') + \mathbf{\Omega}_j(t') \cdot [\mathbf{v}_i(t) - \mathbf{u}_j(t')]. \quad (7)$$

$\mathbf{\Omega}_j(t')$  is a rotation matrix, which is independently chosen at random for each time step and each cell. We use rotations about one of the coordinate axes by an angle  $\pm\alpha$ , with  $\alpha$  fixed. The coordinate axis as well as the sign of the rotation are chosen at random, resulting in 6 possible rotation matrices. To remove anomalies introduced by the regular grid, one can either choose a mean free path of the order of the cell size or shift the whole grid by a random vector once per SRD time step as proposed by Ihle and Kroll [47,48].

Three different methods to couple the SRD and the MD simulation have been introduced in the literature. Inoue et al. proposed a way to implement no slip boundary conditions on the particle surface [40]. Padding and Louis very recently came up with full slip boundaries, where the fluid particles interact via Lennard-Jones potentials with the colloidal particles [49]. Falck et al. [50] have developed a “more coarse grained” method which we use for the simulations of the present paper and which we describe shortly in the following.

To couple the colloidal particles to the fluid, the colloidal particles are sorted into the SRD cells and their velocities are included in the rotation step. One has to use the mass of each particle—colloidal or fluid particle—as a weight

factor when calculating the mean velocity

$$\mathbf{u}_j(t') = \frac{1}{M_j(t')} \sum_{i=1}^{N_j(t')} \mathbf{v}_i(t) m_i, \quad (8)$$

$$\text{with } M_j(t') = \sum_{i=1}^{N_j(t')} m_i, \quad (9)$$

where we sum over all colloidal and fluid particles in the cell, so that  $N_j(t')$  is the total number of both particles, fluid plus colloidal ones.  $m_k$  is the mass of the particle with index  $i$  and  $M_j(t')$  gives the total mass contained in cell  $j$  at time  $t' = t + \tau$ . In summary, the algorithm for the fluid simulation is described by Eqns. (6)–(9). To some of our simulations we apply shear. This is realized by explicitly setting the mean velocity  $\mathbf{u}_j$  to the shear velocity in the cells close to the border of the system. Both, colloidal and fluid particles, are involved in this additional step. A thermostat is applied to remove the energy introduced to the system by the shear force. We have described the simulation method in more detail in Ref. [25,26].

### 3 Simulation Setup

In this study the colloidal particles are represented by three dimensional spheres of  $d = 0.37 \mu\text{m}$  in diameter. This is the mean diameter of the particles used in the experiments to which we refer in Ref. [26]. We have simulated a small volume,  $24d = 8.88 \mu\text{m}$  long in  $x$ -direction, which is the shear direction, and  $12d = 4.44 \mu\text{m}$  long in  $y$ - and  $z$ -direction. We have varied the volume fraction between  $\Phi = 10\%$  (660 particles) and  $\Phi = 40\%$  (2640 particles). Most of the simulations were performed at  $\Phi = 35\%$  (2310 particles). We use periodic boundaries in  $x$ - and  $y$ -direction and closed boundaries in  $z$ -direction. The  $xy$ -plane is our shear plane. For simulations without shear, to achieve the best comparability, we use the same boundary conditions and just set the shear rate to  $\dot{\gamma} = 0$ . In addition we have performed simulations with two different shear rates: with  $\dot{\gamma} = 100/\text{s}$  and with  $\dot{\gamma} = 500/\text{s}$ . The dimensionless Peclét numbers are  $Pe = 3$  and  $Pe = 15$ , respectively.

## 4 Results and Discussion

### 4.1 Correlation function

First, we focus on simulations without shear. The pair correlation function

$$g(r) = \frac{V}{N^2} \left\langle \sum_i \sum_{j \neq i} \delta(r - r_{ij}) \right\rangle, \quad (10)$$

(see Ref. [32] p.55), where  $V$  is the volume,  $N$  the number of particles and  $r_{ij}$  the distance of two particles  $i$  and  $j$ , can be used for a first characterization of the system. Depending on the  $p\text{H}$ -value the behavior of the system changes from a repulsive structure around  $p\text{H} = 4$ ,  $I = 3 \text{ mmol/l}$  to a stable suspension around  $p\text{H} = 6$ ,  $I = 3 \text{ mmol/l}$  towards a clustered region if the  $p\text{H}$ -value is increased, until the isoelectric point is reached at  $p\text{H} = 8.7$ , where clustering occurs in any case, independent on the ionic strength. Electrostatic repulsion prevents clustering (at  $p\text{H} = 4$ ). Particles are suspended, and there is no fixed long range ordering in the system. The correlation function (Fig. 1) shows a maximum at a typical nearest neighbor distance slightly above  $\frac{r}{d} = 1$  with  $d$  denoting the particle diameter, then in the layer of next neighbors small correlations can be found (at  $\frac{r}{d} = 2$ ). For larger distances the correlation function is rather constant.

When the  $p\text{H}$ -value is increased, the surface charge is lower, which at first causes the particles to approach each other more closely. The maximum of the correlation function is shifted to smaller distances (see Fig. 1, note that the curves are shifted vertically in the plot by a factor of 3 for better visibility.). Then, van der Waals attraction becomes more important and clustering begins. One can see this in the correlation function where a sharp structure at particle distances between 1.5 and 2 particle diameters occurs. In a solid like cluster the position of the next neighbor is fixed more sharply than in the suspension, consequently the nearest neighbor peak becomes sharper, too, and its height is increased. Close to the isoelectric point ( $p\text{H} = 8.7$ ) the barrier between primary and secondary minimum disappears. The particles, once clustered, cannot rearrange anymore, and therefore the correlations to the next neighbors become less sharp again.

Instead of varying the  $p\text{H}$ -value, one can also vary the ionic strength to achieve similar effects. Increasing the ionic strength, experimentally speaking “adding salt” decreases the screening length  $1/\kappa$  and therefore the attractive forces become more important: the particles start to form clusters. On the contrary, if the ionic strength is decreased—experimentally speaking a dialysis step is performed—the electrostatic repulsion prevents cluster formation and, for sufficiently strong repulsion, long range correlations occur starting at a certain volume fraction.

In Fig. 2 one can see clustering in the primary minimum of the potential as well as in the very shallow secondary minimum. The correlation function plotted there is evaluated after 1000 SRD time steps in a simulation for

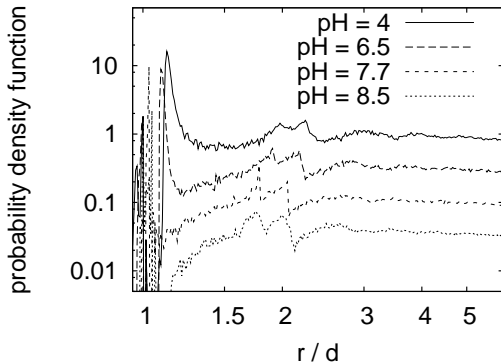


**Figure 1.** Dependence of the particle correlation function on the pH value,  $I = 3$  mmol,  $\dot{\gamma} = 0/s$   $\Phi = 35\%$ . The plots for four different pH-values are shifted against each other for better visibility by a factor of 3. For  $pH = 4$  the particles are not clustered. Hence the structure at  $\frac{r}{d} = 2$  is less sharp than in the other three curves of the plot and the nearest neighbor peak (at  $\frac{r}{d} = 1$ ) is broad. For  $pH = 6.5$  slight clustering starts, the structures become sharper. For  $pH = 7.7$  strong cluster formation is reflected in very sharp structures. For  $pH = 8.5$  electrostatic repulsion nearly disappears so that no barrier between primary and secondary minimum exists anymore. The particles cannot rearrange anymore, and therefore the structures at  $\frac{r}{d} = 2$  become less sharp again.

$pH = 7$  and  $I = 3$  mmol/l at a volume fraction of  $\Phi = 35\%$  sheared with  $\dot{\gamma} = 100/s$ . Note that the shear flow is not of essential importance here, but it supports the particles to overcome the potential barrier between the primary and the secondary minimum. The dotted lines in Fig. 2 denote the zero line.

A secondary minimum only exists if the screening length of the electrostatic repulsion is short enough, i.e., if the ionic strength is large enough. According to the depth of the potential, clustering in the primary minimum is associated with much stronger forces than in the secondary minimum.

The effects described up to here can be seen with or without shear qualitatively in an analogous manner. If the suspension is sheared clustering occurs at higher pH-values and the peaks found in the correlation function are slightly broadened, because the relative particle positions are less fixed. But a new feature appears, if a stable suspension at not too high volume fraction is sheared. Induced by the shear particles arrange themselves in layers. Regular nearest neighbor distances in the shear plane cause the correlation function to become more structured even for large distances (see Fig. 3). The long range structure of the pair correlation function appears after a transient time the particles need to ar-

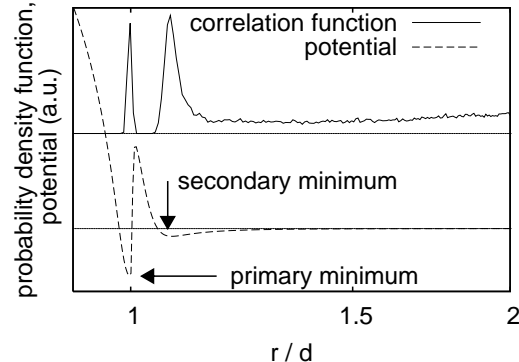


**Figure 2.** Correlation function,  $\dot{\gamma} = 100/s$ ,  $pH = 7$ ,  $I = 3$  mmol/l,  $\Phi = 35\%$ : one finds clustering in the primary and the secondary minimum. Note: The vertical axis is logarithmic, and a constant offset has been added before plotting. Thereby, the coincidence of the minima in the potential with the maxima in the correlation function becomes more apparent. The dotted lines denote the position of the base line before shifting.

range themselves in the layered structure. The curves in Fig. 3 correspond to the same simulation, but for increasing time from bottom to top. The arrows from the bottom indicate the position of the next-neighbor peak and the next-next-neighbors (Since the particles do not touch each other, the peaks are located not exactly at  $\frac{r}{d} = 1, 2, 3, \dots$ ). Within one layer which moves as a whole, a hexagonal particle order appears, which can be seen in the occurrence of a peak at  $\frac{r}{d} = \sqrt{3}$  times the position of the nearest neighbor peak, i.e., the next neighbor peak splits, as indicated by the arrows from above. The same applies to the next-next neighbor peak marked by the second set of arrows at  $3 < r/d < 4$ .

We have integrated over the nearest neighbor peaks, both, the peaks of the primary and the secondary minimum, and plotted the integral versus pH-value in Fig. 4. We have chosen  $I = 3$  mmol/l and  $\Phi = 35\%$  and three different shear rates:  $\dot{\gamma} = 0, 100$  and  $500/s$ . We have integrated the correlation function for  $r < 1.215d$ , where for all pH-values the potential in the secondary minimum has a value of  $-\frac{1}{2}k_B T$ . In other words, we have captured the primary and the secondary minimum of the potential for this plot. For low pH-values clustering (in the secondary minimum) is only possible for low shear rates. For high shear rates, the hydrodynamic forces do not allow the formation of stable clusters. For rising pH-values the clustering increases, first for the unsheared suspension, at higher pH-values for low shear rates ( $\dot{\gamma} = 100/s$ ) and finally for high shear rates ( $\dot{\gamma} = 500/s$ ). Remarkably, for  $pH > 7.5$  the curve for  $\dot{\gamma} = 100/s$  shows stronger cluster formation than the other ones. Particles are

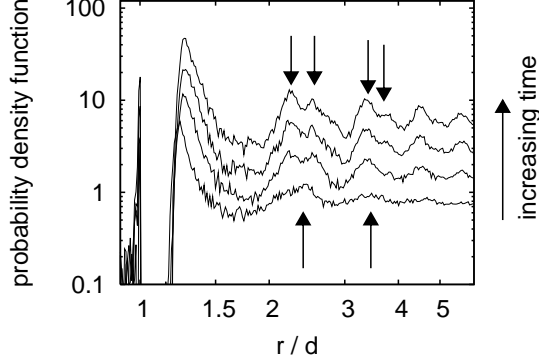


**Figure 3.** Correlation function for  $\dot{\gamma} = 500/s$ ,  $pH = 6$ ,  $I = 0.3 \text{ mmol/l}$ ,  $\Phi = 32\%$ : depending on the simulation time the peaks indicated by the arrows from below split into two (indicated by the arrows from above), and long range correlations occur (for  $\frac{r}{a} > 4$ ). This reflects the process of layer formation and appearing of a regular (hexagonal) order in the layers. From bottom to top several states for increasing time are shown. The plots are shifted vertically by a factor of 2 for better visibility.

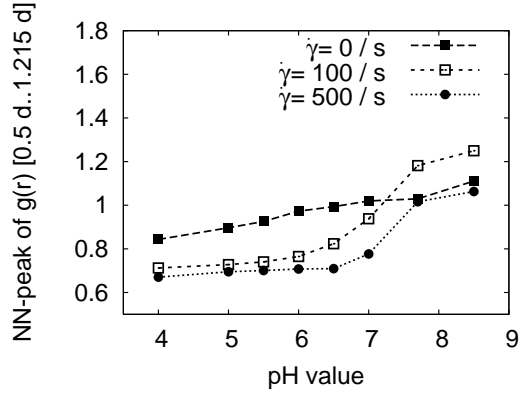


**Figure 4.** Nearest neighbor peak (primary and secondary minimum of the potential) of the correlation function  $I = 3 \text{ mmol/l}$ ,  $\Phi = 35\%$ : For low  $pH$ -values clustering is prevented by the electrostatic repulsion. For high  $pH$ -values the particles form clusters, which is reflected by an increased nearest neighbor peak. First, shear prevents clustering, then depending on the shear rate, cluster formation takes place. Low shear rates even support cluster formation at high  $pH$ -values.

brought together by the shear flow, so that compared to the case of no shear, the clustering process is supported here. On the other hand, the shear stress may not be too strong, because otherwise the clustering process is limited by the shear flow again (for  $\dot{\gamma} = 500/s$  the clustering is less pronounced than for  $\dot{\gamma} = 100/s$ ).

## 4.2 Structure Factor

Closely related to the pair correlation function is another important analysis tool: the structure factor, defined by

$$S(\mathbf{k}) = \frac{1}{N} \sum_{l,m=1}^N \exp(i\mathbf{k} \cdot \mathbf{r}_{lm}), \quad (11)$$

where  $N$  is the number of particles, and  $\mathbf{r}_{lm}$  is the vector from particle  $l$  to particle  $m$ .  $i$  denotes the imaginary unit here. The structure factor is defined in  $\mathbf{k}$ -space and it is related to the pair correlation function in real space by a three dimensional Fourier transform:

$$S(k) - 1 = \int d\mathbf{r} \exp(i\mathbf{k} \cdot \mathbf{r}) \rho g(r), \quad (12)$$

with the density  $\rho$ . In scattering experiments it can be extracted from the scattered intensity  $I'$  [51], which is proportional to the incident intensity  $I(\mathbf{k})$ , to the volume fraction  $\Phi$ , and to  $S(\mathbf{q})$ , where  $\mathbf{q} = \mathbf{k}' - \mathbf{k}$  is the so called scattering vector:

$$I'(\mathbf{k}') \sim I(\mathbf{k}) S(\mathbf{q}) P(\mathbf{q}) \Phi. \quad (13)$$

$P(\mathbf{q})$  is the form factor, which describes the influence of the particle shape. In diluted suspensions the form factor dominates the dependency  $I'(\mathbf{k}')$ , whereas in dense suspensions, where particles influence each other, the information about the local order is expressed by the additional structure factor  $S(\mathbf{q})$ .

Unfortunately scattering experiments of suspensions like we focus on, face severe problems. The suspension is not transparent enough for light scattering and the particles are too large for X-ray scattering experiments. Additionally separating the different influences to the scattering intensity poses difficulties. Especially the form factor has to be divided out. Therefore excellent measurements of the scattering intensity would be necessary.

However, from our simulations we can extract the structure information directly. In this sense the structure factor can be seen as a tool for quantitative analysis of the simulated system without facing the problems which arise when analyzing experimental scattering data. For illustration we can qualitatively compare our simulations to experimental results for different materials or to different simulation results in the literature. Similar peaks of the structure factor are reported by many authors, e.g., in Ref. [52] for a 2D system of Lennard Jones disks, and in Ref. [53] for a 3D system at low volume fractions.

In simulations one can directly evaluate  $S(k)$  according to Eq. (11). A peak at a certain  $\mathbf{k}$ -vector corresponds to a typical particle center center distance  $r_{ij} = \frac{2\pi}{k}$  occurring frequently in the

system. One typical length for dense systems is about one particle diameter, the distance particle centers have to keep so that they do not overlap. The corresponding peak of the structure factor is the nearest neighbor peak at  $k = \frac{2\pi}{d}$ . In a single crystal the peak would be sharp, since the particle positions are well defined, whereas in our case of a suspension there is a certain disorder, which broadens the peak.

Similar to the nearest neighbor peak another peak can be detected at twice the  $\mathbf{k}$ -vector, which corresponds to a distance of one particle radius. This does not necessarily mean that there are particles whose centers are only one particle radius apart. It only means that for a certain  $\mathbf{k}$ -vector the addends in Eq. (11) do not cancel out each other. In fact, this peak can be seen in experiments with latex particles [54,55], where the interactions can be described by DLVO theory, too. As in our case, the particle suspensions are stabilized by a surface charge, which can be screened by increasing the ionic strength of the solvent. The samples can be observed via light scattering.

For small  $\mathbf{k}$ -vectors there is another peak, or in our case an increase of the structure factor towards low  $\mathbf{k}$ -vectors. The length scale corresponds to the size of the whole system. If large clusters are formed, this can be seen in an increase of the low- $\mathbf{k}$ -peak, since the contributions on this length scale do not cancel out each other anymore. This can be used in experiments to detect clustering or gelation, provided that the resolution of the measuring device allows to detect the respective  $\mathbf{k}$ -vectors. In Ref. [56] and [57] Shah et al. report on their observations of depletion driven gelation of a colloid polymer mixture using X-ray scattering. Their samples show a strong increase of the low- $\mathbf{k}$ -peak as soon as it undergoes the sol-gel transition.

Even though the mechanism for the attractive interaction is different from our system, the resulting structure is comparable to what we find. Fig. 5 illustrates the similarities of the structure factor of one of our simulations ( $pH = 6$ ,  $I = 15 \text{ mmol/l}$ ,  $\Phi = 35\%$ ,  $\dot{\gamma} = 100/\text{s}$ ) with experimental data taken from Ref. [57]. The structure factor was extracted from ultra small angle x-ray scattering at silica colloidal particles of  $R = 59 \pm 3 \text{ nm}$  in a polystyrene solution. The measurements show a nearest neighbor peak at the same position (marked by the arrow) as our data, which is typical for dense solutions. The “lift-up” at low  $\mathbf{k}$ -vectors as well can be seen in both, simulation and measurements. Of course, the agreement is not perfect, since we did not adjust our simulation parameters explicitly to this experimental situation. Fig. 5 is meant as an illustration only.

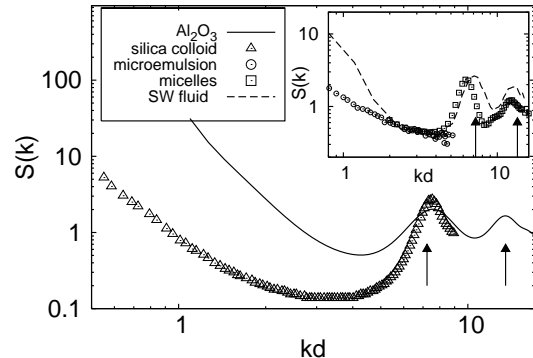


**Figure 5.** Comparison with literature and experimental data: main figure: Our simulation for  $pH = 6$ ,  $I = 15 \text{ mmol/l}$ ,  $\Phi = 35\%$ . The triangles are ultra small angle x-ray scattering data taken from Ref. [57], Fig. 7b). The sample was a depletion induced gel of silica colloidal particles of  $R = 59 \pm 3 \text{ nm}$  in a polystyrene solution. The arrows mark the position of the nearest neighbor peak and the  $2^{nd}$ -order-peak respectively. The same arrows are shown again in the inset, where we have plotted structure factor data taken from the literature: The dashed line is a Newtonian simulation of a binary mixture of spheres interacting with square well potentials taken from Ref. [58], Fig. 9b). The circles are experimental data extracted from small angle neutron scattering (SANS) experiments (taken from Ref. [59], Fig. 2b)). The system was a three-component microemulsion consisting of small water droplets (radius  $R = 60 \text{ \AA}$ ) coated with a layer of surfactant and suspended in oil. The volume fraction was  $\Phi = 7.5\%$ . The squares represent SANS data taken from Ref. [60], Fig. 4) for starlike block copolymer micelles.

It is difficult to gain accurate structure factors on the whole range from low  $\mathbf{k}$ -vectors corresponding to cluster sizes or even the size of the whole system up to higher order peaks. Therefore we have collected two more examples for the measurement of structure factors in the inset of Fig. 5: The low- $\mathbf{k}$ -peak can be seen in small angle neutron scattering (SANS) data of a microemulsion taken from Ref. [59]. Small water droplets (radius  $R = 60 \text{ \AA}$ ) coated with a layer of surfactant were suspended in oil at a volume fraction of  $\Phi = 7.5\%$ . The nearest neighbor peak and the  $2^{nd}$ -order-peak can be seen in SANS data taken from Ref. [60] where structures formed by starlike block copolymer micelles were investigated. The shift to smaller  $\mathbf{k}$ -vectors (compare the position of the peaks relative to the arrows) reflects the larger inter particle distances caused by the polymers attached to the core. To finish with this illustration, the dashed line finally is data of a Newtonian simulation taken from Ref. [58]. In this case a binary mixture of spheres interacting with square well potentials has been investi-

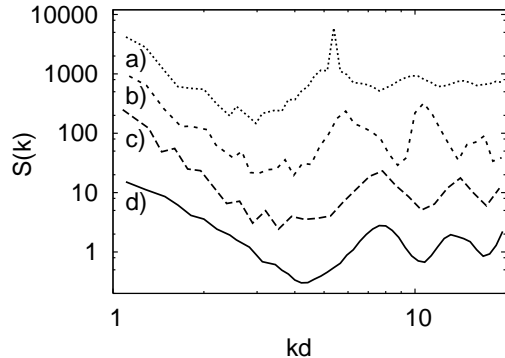


**Figure 6.** Structure factor for some selected examples, with  $pH = 6$  fixed for all plots:  $\dot{\gamma} = 500/s$ ,  $I = 0.3 \text{ mmol/l}$ : a)  $\Phi = 20\%$  and b)  $\Phi = 35\%$ ,  $\dot{\gamma} = 0$ ,  $I = 25 \text{ mmol/l}$ : c)  $\Phi = 40\%$  and d)  $\Phi = 10\%$ . The curves are shifted vertically for better visibility. In case a) ten layers can be identified in the system, resulting in the strong peak close to 5. But, since the particles in the layers can still move freely, there is no  $2^{nd}$ -order-peak. In case b) layers are formed, but particles are moving from one layer to the other, disturbing the flow. As a result the nearest neighbor peak is much broader. Due to the structure in the layers, a  $2^{nd}$ -order-peak appears. In case c) the interaction is strongly attractive, hence the particles approach each other and the nearest neighbor peak is shifted to higher  $\mathbf{k}$ -vectors. In case d) the volume fraction is much less. The slope of the low- $\mathbf{k}$ -peak is much flatter, which means that the cluster is fractal.

gated. All the previously discussed features are present in the structure factor of this simulation.

In Fig. 6 we have plotted several typical structure factors of our simulations. For these plots the  $pH$ -value is fixed to  $pH = 6$ . The cases a) and b) are sheared with  $\dot{\gamma} = 500/s$  at an ionic strength of  $I = 0.3 \text{ mmol/l}$ . In case a) the volume fraction  $\Phi = 20\%$  is relatively low. Therefore the particles can arrange themselves in layers parallel to the shear plane, which move relatively independently in the shear flow. They have a certain distance fixed in space and time. This can be seen in a sharp peak at a dimensionless  $\mathbf{k}$ -vector of  $k = 5.2$ , which corresponds to a distance of 1.2 particle diameters. In fact, this is exactly the distance between two neighboring layers, as one can easily verify by counting the layers in a snapshot of the system (Fig. 7a)). The particles in the layers do not have a fixed distance and therefore no  $2^{nd}$ -order-peak can be observed.

For case b) the volume fraction is increased to  $\Phi = 35\%$ . The particle layers are packed more densely and therefore the interactions between one layer and the neighboring one become relevant. Particles jump from one layer to the other, which disturbs the flow and therefore the dis-

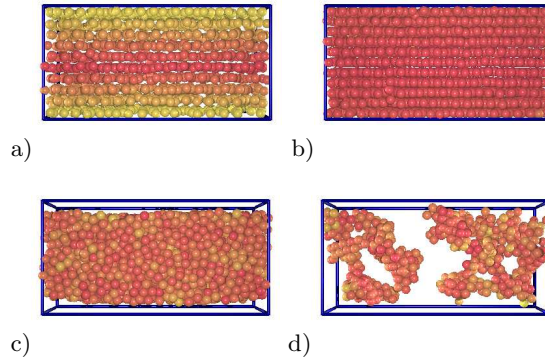


**Figure 7.** Images of the systems for Fig. 6: In case a) one can see the layers resulting in the sharp peak in the structure factor. In case b) the layers are packed closer due to the higher volume fraction. Collisions between particles of neighbouring layers happen more frequently. In case c) one big cluster is formed. The particles are packed densely. In case d) the fractal nature of the system can be seen directly.

tance between the layers is not fixed anymore. The sharp peak on the nearest neighbor peak disappears. Instead of that, in each layer a regular hexagonal order appears and therefore the  $2^{nd}$ -order-peak is much more pronounced.

In case c) the ionic strength is increased to  $I = 25 \text{ mmol/l}$ . The inter-particle potentials are attractive, hence cluster formation takes place. In this simulation we did not apply shear, therefore one finds only one big cluster in the system (compare Fig. 7c)). In the cluster the particles are packed more densely and consistently the nearest neighbor peak in the structure factor is shifted to larger  $\mathbf{k}$ -vectors. The volume fraction is  $\Phi = 40\%$  in this case.

In case d) the volume fraction is decreased to  $\Phi = 10\%$ . The particles still form clusters, but their mobility is not high enough to create one compact cluster. The system is rather fractal (see Fig. 7d)). This can be seen in the structure factor as well: The slope of the low- $\mathbf{k}$ -peak is flatter in this case compared to the cases a)–c). A flatter slope of the low- $\mathbf{k}$ -peak is typical for structure factors of fractal objects. Lattuada et al. [51] have evaluated the fractal dimension of agglomerates of latex particles from the slope of the structure factor. McCarhy et al. [61] give an introduction to scattering intensities at fractal objects, without mentioning the structure factor, but their arguments refer to the contribution of the structure factor on the scattering intensity.

Differing from experiments and from other simulations, we can always find a low- $\mathbf{k}$ -peak, not only if the system clusters. The reason for this is that we have closed boundary conditions in  $z$

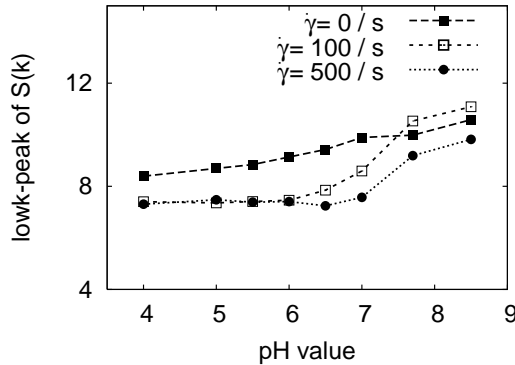


**Figure 8.** low- $\mathbf{k}$ -peak for different  $p\text{H}$ -values and different shear rates. The ionic strength  $I$  is kept constant at  $I = 3$  mmol/l and the volume fraction is always  $\Phi = 35\%$ . For  $\dot{\gamma} = 0/\text{s}$  the particles tend to cluster in the secondary minimum of the potential. This clustering can easily be broken up, if shear is applied. If the  $p\text{H}$ -value is increased, shear cannot prevent cluster formation anymore. At low shear rates ( $\dot{\gamma} = 100/\text{s}$ ) clustering is even enhanced, since the particles are brought closer to each other by the shear flow.

direction which confines the particle positions in  $z$  direction so that the particles do not stick out of the system in  $z$  direction. In Fig. 8 we have shown the dependence of the low- $\mathbf{k}$ -peak of the structure factor on the  $p\text{H}$ -value. Here we have integrated over dimensionless  $\mathbf{k}$ -vectors smaller than 3 which means, we have captured structures larger than twice a particle diameter. A large integral over the low- $\mathbf{k}$ -peak is due to a large inhomogeneity in the system. In one part of the system particles are present and in the other part not. In other words, we observe the process of cluster formation on a length scale of the system size. Without shear, particles cluster in the secondary minimum for all  $p\text{H}$ -values. If the system is slightly sheared ( $\dot{\gamma} = 100/\text{s}$ ) clustering is suppressed for low  $p\text{H}$ -values. Starting at  $p\text{H} = 6$  the cluster formation starts and is even supported by the shear flow for  $p\text{H}$ -values larger than 7.5. For large shear rates ( $\dot{\gamma} = 500/\text{s}$ ) the cluster formation is suppressed by the shear flow. By analyzing the low- $\mathbf{k}$ -peak of the structure factor one observes on the length scale of the system size. The same behavior of the system can be seen by analyzing the pair correlation function, as we have already shown in Fig. 4. In that case one analyzes the number of nearest neighbors, that means, one observes the length scale of a particle diameter. Nevertheless, both graphs show the same behavior of the system, i.e., we have a consistent picture of the cluster formation process on the length scale of the nearest neighbors and on the length scale of the system size.

### 4.3 Density Inhomogeneity

Another way to observe the cluster formation process is provided by the “demixing parameter” defined in Ref. [29]. The system is divided into  $n^3$  cubes and the particle density  $\rho_k$  is evaluated in each cube. The demixing parameter is the mean squared deviation of the density

$$\Psi_n = \sum_{k=0}^{n^3} (\rho_k - \bar{\rho})^2, \quad (14)$$

where  $\bar{\rho}$  is the mean density. For our elongated system we modify this definition and use  $2n$  cubes in  $x$ -direction, resulting in  $2n^3$  cubes in total. In Fig. 9 we have plotted the demixing parameter  $\Psi_4$  versus time for three different shear rates and four different ionic strengths in each plot. The  $p\text{H}$ -value is kept constant at  $p\text{H} = 6$  and the volume fraction at  $\Phi = 35\%$ . Without shear  $\Psi_4$  is nearly constant. Even if a cluster is formed, it does not move, so that the average density in the boxes does not change much. For lower volume fractions the time dependence without shear is stronger. If shear is applied the clusters are deformed so that stronger inhomogeneities appear. Depending on the ionic strength the demixing parameter increases with cluster formation (high ionic strength) or still stays constant when the interactions are repulsive (low ionic strength). For  $\dot{\gamma} = 100/\text{s}$  the strongest cluster formation is achieved for the highest ionic strength  $I = 20$  mmol/l. If the ionic strength is decreased, the clustering effect decreases as well, until it disappears completely at  $I = 1$  mmol/l, where the repulsive regime is reached. To see the shear rate dependence, compare the plots for  $\dot{\gamma} = 100/\text{s}$  and  $500/\text{s}$ . If the shear rate is increased, the cluster formation starts faster because the shear flow brings the particles faster in contact, but the resulting inhomogeneity of the final state is less than for lower shear rates. This shows again the crossover for nonzero shear rates in Fig. 4 and Fig. 8. Additionally, Fig. 9 shows the time evolution.

### 4.4 Repulsive Regime

To characterize the repulsive regime, we have evaluated the mean squared displacement for the particles. In Fig. 10 we have plotted the mean squared displacement for different ionic strengths. The  $p\text{H}$ -value is kept constant at  $p\text{H} = 6$  and the volume fraction is  $\Phi = 35\%$  for this plot. Three different regimes can be identified. For very short times, the ballistic regime: particles move on short distances without a notable influence by their neighbors. The distances are in

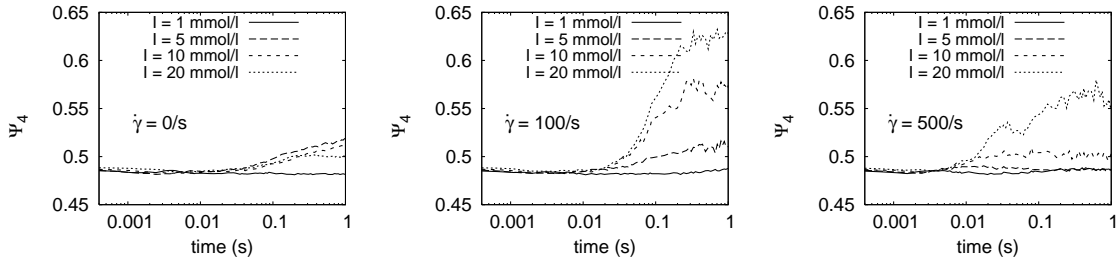


**Figure 9.** Demixing parameter for constant  $pH = 6$  and volume fraction  $\Phi = 35\%$  for three different shear rates:  $\dot{\gamma} = 0/s$  (left),  $100/s$  (center) and  $500/s$  (right). Without shear only very weak demixing takes place. For  $\dot{\gamma} = 100/s$  the strongest demixing can be observed for the system with the highest ionic strength  $I = 20$  mmol/l. For lower ionic strengths the effect decreases until it disappears completely at  $I = 1$  mmol/l, where the repulsive regime is reached. If the shear rate is further increased ( $\dot{\gamma} = 500/s$ ), the clusters are less stable so that the system becomes less inhomogeneous. For  $I = 5$  mmol/l the demixing is even suppressed completely.

the order of some percent of the particle diameter and the times are a few SRD time steps. For larger times the particles interact with their neighbors and therefore their mobility is limited. Collisions with the neighbors reduce the slope of the mean squared displacement. For even larger time scales collective motion starts, i.e., clusters or groups of particles move, or single particles can escape from a cage formed by its neighbors. Depending on the ionic strength the shape of the curve is different. For large ionic strengths the particles form clusters and these clusters may drift or rotate in the system. Then the collective motion is more dominant and the mean squared displacement grows faster than in single particle diffusion. The mean squared displacement does not show a plateau, then. But in the repulsive regime, the neighbors limit the motion of the particles, and the slope of the plateau is flatter, i.e., the plateau is even more pronounced, compared to the suspended case.

#### 4.5 Stability Diagram

The results of the investigations presented in this paper can be summarized in a stability diagram for our  $Al_2O_3$ -suspension (Fig. 11). Three different microstructures can be identified: a repulsive structure, a suspended region and a clustered region. In contrast to our previous work [25,26], we have explored the parameter space more in the repulsive regime and deeper in the clustered region. We use the mean squared displacement, the demixing parameter  $\Psi$  [29], the correlation function, and the structure factor, to decide to which of the three microstructures a certain point in the stability diagram belongs. However, since the borders are not sharp, the assignment is not always totally clear, and one has to consider several criteria. To decide if a state is in the suspended region or in the repulsive

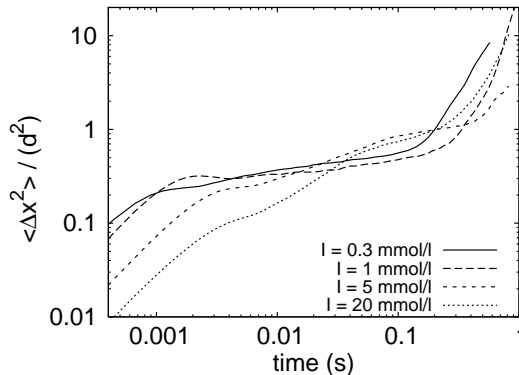


**Figure 10.** Mean squared displacement at  $pH = 6$  for different ionic strengths, without shear. One can see a ballistic regime for short times, a central plateau and a collective long time movement, which can be a movement of a whole cluster or cage escape events of single particles. Depending on the ionic strength, the central plateau is more or less pronounced. A comparison of the plateau for different simulations can be used to decide, if a certain state belongs to the repulsive state region of the stability diagram. A state well in the liquid microstructure should be used as a reference for the comparison.

region of the stability diagram, we have compared the plots of the mean squared displacement by eye. If the plateau was pronounced, we have counted the state among the repulsive regime. To achieve reliable results from the calculation of the mean squared displacement one has to restrict oneself to the unsheared case. However, without shear weak clustering can be seen in the suspended case as well, since there is no barrier for the particles to enter the secondary minimum, but the clusters can be broken up again very easily. Therefore, we also look at the density of the clusters and the time it takes to form them. These values are indications for their stability, and so we allow slight clustering

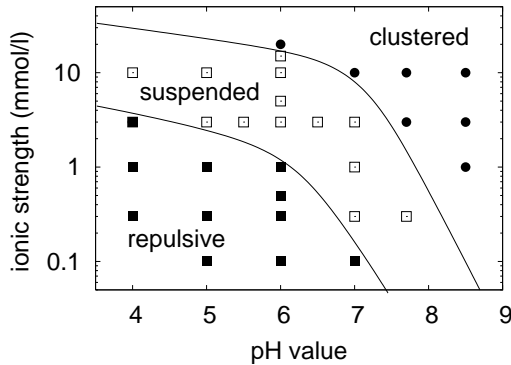


**Figure 11.** Stability diagram (plotted for  $\Phi = 35\%$  and without shear): depicting three regions: a clustered region (filled circles), a suspended regime (open squares), and a repulsive structure (filled squares). The borders are not sharp. They depend on the shear rate and on the volume fraction. The lines are guides to the eye.

in the suspended regime. If one compares with the simulations with shear flow, as in Fig. 4 and Fig. 8 it is reasonable to draw the border this way, keeping in mind that it is shifted slightly according to the applied shear rate.

## 5 Summary and Outlook

We have simulated colloidal particles in shear flow and investigated how the clustering process due to attractive DLVO potentials is affected by the hydrodynamic forces. We find a consistent behavior on different length scales. The pair correlation function has been used to observe the direct neighborhood of the particles and the structure factor to keep track of the length scales up to the system size. In both cases a suppression of the cluster formation by the shear flow can be seen at low  $pH$ -values. For large  $pH$ -values low shear rates even support the clustering process. In contrast, for high shear rates it suppresses the cluster formation. We have evaluated the mean squared displacement and the demixing parameter  $\Psi$  [29] in order to draw the stability diagram as given in Fig. 11. This stability diagram is reproduced quantitatively for the first time from simulations. It helps to predict the behavior of a real suspension. Our findings on the cluster formation process suggest that soft stirring can enhance the cluster formation in industrial processing of this material. The structure factor can experimentally be measured only with difficulties for our system, but from our simulations we can extract it and analyze the structure of the suspension. Further investigations can be carried out on the fractal dimension and its dependence on the experimental conditions. The

cluster size distribution could as well deliver interesting insights useful to design industrial processes.

## Acknowledgements

This work has been financed by the German Research Foundation (DFG) within the project DFG-FOR 371 “Peloide”. We thank G. Gudehus, G. Huber, M. Külzer, L. Harnau, M. Bier, J. Reinshagen, and S. Richter for valuable collaboration.

This work is resulting in large parts from the collaboration with the group of A. Coniglio, Università di Napoli “Federico II”, Naples, Italy. M. Hecht thanks him and his group for his hospitality and for the valuable support during his stay there. M. Hecht thanks the DAAD for the scholarship (Doktorandenstipendium) which enabled him the stay.

The computations were performed on the IBM p690 cluster at the Forschungszentrum Jülich, Germany and at HLRS, Stuttgart, Germany.

## References

1. A.J.C. Ladd, *J. Fluid Mech.* **271**, 285 (1994)
2. A.J.C. Ladd, *J. Fluid Mech.* **271**, 311 (1994)
3. T.N. Phung, J.F. Brady, G. Bossis, *J. Fluid Mech.* **313**, 181 (1996)
4. L. E. Silbert, J. R. Melrose, R. C. Ball, *Phys. Rev. E* **56**(6), 7067 (1997)
5. L. Harnau, S. Dietrich, *Phys. Rev. E* **69**, 051501 (2004)
6. E.J.W. Verwey, J.T.G. Overbeek, *Theory of the Stability of Lyophobic Colloids* (Elsevier, Amsterdam, 1948)
7. B.V. Derjaguin, L.D. Landau, *URSS* **14**, 633 (1941)
8. S. Alexander, P.M. Chaikin, P. Grant, G.J. Morales, P. Pincus, D. Hone, *J. Chem. Phys.* **80**(11), 5776 (1984)
9. M.J. Grimson, M. Silbert, *Macromol. Phys.* **74**(2), 397 (1991)
10. R. van Roij, J.P. Hansen, *Phys. Rev. Lett.* **79**(16), 3082 (1997)
11. J. Dobnikar, Y. Chen, R. Rzehak, H.H. von Grünberg, *J. Phys.: Condens. Matter* **15**, S263 (2003)
12. V. Trappe, V. Prasad, L. Cipelletti, P.N. Segre, D.A. Weitz, *Nature* **411**(3), 772 (2001)
13. Y. Levin, T. Trizac, L. Bocquet, *J. Phys.: Condens. Matter* **15**, S3523 (2003)
14. A.P. Hynninen, M. Dijkstra, R. van Roij, *Phys. Rev. E* **69**, 061407 (2004)
15. N. Sator, E. del Gado, A. Coniglio, *Physica A* **358**, 239 (2005)
16. J. Dobnikar, R. Rzehak, H.H. von Grünberg, *Europhys. Lett.* **61**(5), 695 (2003)

17. T. Palberg, W. Mönch, F. Bitzer, R. Piazza, T. Bellini, *Phys. Rev. Lett.* **74**, 4555 (1995)
18. R. Yamamoto, K. Kim, Y. Nakayama, K. Miyazaki, D.R. Reichman, arXiv: condmat/0604404 (2006)
19. W.B. Russel, D.A. Saville, W. Schowalter, *Colloidal Dispersions* (Cambridge Univ. Press., Cambridge, 1995)
20. G. Lagaly, O. Schulz, R. Zimehl, *Dispersionen und Emulsionen* (Dr. Dietrich Steinkopff Verlag, Darmstadt, Germany, 1997)
21. I.D. Morrison, S. Ross, *Colloidal Dispersions: Suspensions, Emulsions and Foams* (John Wiley and Sons, New York, 2002)
22. R.J. Hunter, *Foundations of colloid science* (Oxford University Press, 2001)
23. R. Oberacker, J. Reinshagen, H. von Both, M.J. Hoffmann, *Ceramic Transactions* **112**, 179 (2001)
24. J. Reinshagen, R.C.D. Cruz, R. Oberacker, J. Hoffmann, to be submitted (2006)
25. M. Hecht, J. Harting, T. Ihle, H.J. Herrmann, *Phys. Rev. E* **72**, 011408 (2005)
26. M. Hecht, J. Harting, M. Bier, J. Reinshagen, H.J. Herrmann, arXiv: condmat/0601413 (2006)
27. A. Malevanets, R. Kapral, *J. Chem. Phys.* **110**, 8605 (1999)
28. A. Malevanets, R. Kapral, *J. Chem. Phys.* **112**, 7260 (2000)
29. A.M. Puertas, M. Fuchs, M.E. Cates, *Phys. Rev. E* **67**, 031406 (2003)
30. M. Smoluchowski, *Bulletin International de l'Academie des Sciences de Cracovie* **8**, 182 (1903)
31. M. Hütter, Ph.D. thesis, Swiss Federal Institute of Technology Zurich (1999)
32. M.P. Allen, D.J. Tildesley, *Computer simulation of liquids*, Oxford Science Publications (Clarendon Press, 1987)
33. J.F. Brady, G. Bossis, *Ann. Rev. Fluid Mech.* **20**, 111 (1988)
34. J.F. Brady, *J. Chem. Phys.* **99**(1), 567 (1993)
35. A. Sierou, J.F. Brady, *J. Fluid Mech.* **448**, 115 (2001)
36. A. Sierou, J.F. Brady, *J. Fluid Mech.* **506**, 285 (2004)
37. M. Hütter, *J. Colloid Interface Sci.* **231**, 337 (2000)
38. A.J.C. Ladd, R. Verberg, *J. Stat. Phys.* **104**(5), 1191 (2001)
39. A. Komnik, J. Harting, H.J. Herrmann, *Journal of Statistical Mechanics: theory and experiment* **P12003** (2004)
40. Y. Inoue, Y. Chen, H. Ohashi, *J. Stat. Phys.* **107**(1), 85 (2002)
41. J.T. Padding, A.A. Louis, *Phys. Rev. Lett.* **93**, 220601 (2004)
42. M. Ripoll, K. Mussawisade, R.G. Winkler, G. Gompper, *Europhys. Lett.* **68**, 106 (2004)
43. R.G. Winkler, K. Mussawisade, M. Ripoll, G. Gompper, *J. Phys.: Condens. Matter* **16**(38), S3941 (2004)
44. I. Ali, D. Marenduzzo, J.M. Yeomans, *J. Chem. Phys.* **121**, 8635 (2004)
45. M. Ripoll, R.G. Winkler, G. Gompper, *Phys. Rev. Lett.* **96**, 188302 (2006)
46. M. Ripoll, K. Mussawisade, R.G. Winkler, G. Gompper, *Phys. Rev. E* **72**, 016701 (2005)
47. T. Ihle, D.M. Kroll, *Phys. Rev. E* **67**, 066705 (2003)
48. T. Ihle, D.M. Kroll, *Phys. Rev. E* **67**, 066706 (2003)
49. J.T. Padding, A.A. Louis, arXiv: condmat/0603391 (2006)
50. E. Falck, J.M. Lahtinen, I. Vattulainen, T. AlaNissila, *Eur. Phys. J. E* **13**, 267 (2004)
51. M. Lattuada, H. Wu, M. Morbidelli, *Phys. Rev. E* **64**, 061404 (2001)
52. B.D. Butler, H.J.M. Hanley, D. Hansen, D.J. Evans, *Phys. Rev. B* **53**(5), 2450 (1996)
53. E. del Gado, W. Kob, *Europhys. Lett.* **72**(6), 1032 (2005)
54. C. Urban, S. Romer, F. Scheffold, P. Schurtenberger, *Progr. Coll. Polym. Sci.* **115**, 270 (2000)
55. L.F. Rojas, C. Urban, P. Schurtenberger, T. Gisler, H.H. von Grünberg, *Europhys. Lett.* **60**(5), 802 (2002)
56. S.A. Shah, S. Ramakrishnan, Y.L. Chen, K.S. Schweizer, C.F. Zukoski, *Langmuir* **19**, 5128 (2003)
57. S.A. Shah, Y.L. Chen, S. Ramakrishnan, K.S. Schweizer, C.F. Zukoski, *J. Phys.: Condens. Matter* **15**, 4751 (2003)
58. G. Foffi, C. De Michele, F. Sciortino, P. Tartaglia, *J. Chem. Phys.* **122**, 224903 (2005)
59. J.S. Huang, S.A. Safran, M.W. Kim, G.S. Grest, M. Kotlarchyk, N. Quirke, *Phys. Rev. Lett.* **53**(6), 592 (1984)
60. M. Laurati, J. Stellbrink, R. Lund, L. Willner, D. Richter, E. Zaccarelli, *Phys. Rev. Lett.* **94**(19), 195504 (2005)
61. D.W. McCarthy, J.E. Mark, D.W. Schaefer, *J. Polym. Sci. B* **36**(7), 1167 (1998)